AGU100 ADVANCING EARTH AND SPACE SCIENCE

Geochemistry, Geophysics, Geosystems

RESEARCH ARTICLE
10.1029/2018GC007620

Special Section:
Magnetism in the Geosciences - Advances and Perspectives

# Measuring, Processing, and Analyzing Hysteresis Data

Greig A. Paterson[1,2,3], Xiang Zhao[4], Mike Jackson[5], and David Heslop[4]

[1]Department of Earth, Ocean and Ecological Sciences, University of Liverpool, Liverpool, UK, [2]Key Laboratory of Earth and Planetary Physics, Institute of Geology and Geophysics, Chinese Academy of Sciences, Beijing, China, [3]Institutions of Earth Science, Chinese Academy of Sciences, Beijing, China, [4]Research School of Earth Sciences, The Australian National University, Canberra, ACT, Australia, [5]Institute for Rock Magnetism, Winchell School of Earth Sciences, University of Minnesota, Minneapolis, MN, USA

**Key Points:**
- Magnetic hysteresis loops are one of the most widely used rock magnetic data types in Earth sciences
- We outline a broad range of strategies to measure better data and more accurately analyze results
- We introduce *HystLab*, a new software package that incorporates these methods and the ability to produce publication-ready figures

**Correspondence to:**
G. A. Paterson,
greig.paterson@liverpool.ac.uk

**Citation:**
Paterson, G. A., Zhao, X., Jackson, M., & Heslop, D. (2018). Measuring, processing, and analyzing hysteresis data. *Geochemistry, Geophysics, Geosystems*, *19*, 1925–1945. https://doi.org/10.1029/2018GC007620

Received 13 APR 2018
Accepted 12 MAY 2018
Accepted article online 8 JUN 2018
Published online 4 JUL 2018



**Abstract** Magnetic hysteresis loops are important in theoretical and applied rock magnetism with applications to paleointensities, paleoenvironmental analysis, and tectonic studies, among many others. Information derived from these data is among the most ubiquitous rock magnetic data used by the Earth science community. Despite their prevalence, there are no general guidelines to aid scientists in obtaining the best possible data and no widely available software to allow the efficient analysis of hysteresis loop data using the most advanced and appropriate methods. Here we outline detrimental factors and simple approaches to measuring better hysteresis data and introduce a new software package called *Hysteresis Loop analysis box* (HystLab) for processing and analyzing loop data. Capable of reading a wide range of data formats, HystLab provides an easy-to-use interface allowing users to visualize their data and perform advanced processing, including loop centering, drift correction, high-field slope corrections, and loop fitting to improve the results from noisy specimens. A large number of hysteresis loop properties and statistics are calculated by HystLab and can be exported to text files for further analysis. All plots generated by HystLab are customizable and user preferences can be saved for future use. In addition, all plots can be exported to encapsulated postscript files that are publication ready with little or no adjustment. HystLab is freely available for download at https://github.com/greigpaterson/HystLab and in combination with our simple measurement guide should help the paleomagnetic and rock magnetic communities get the most from their hysteresis data.

## 1. Introduction

The use of magnetic hysteresis data is prevalent throughout paleomagnetic and Earth science studies. It has applications in fundamental rock magnetism (Krása et al., 2009; Williams et al., 2010), analyzing paleointensity data (Carvallo et al., 2006; Haag et al., 1995; Kissel et al., 2011; Paterson et al., 2016, 2017), paleoclimate and paleoenvironmental studies (Chang et al., 2016; Hatfield et al., 2017; Liu et al., 2015; R. Zhang et al., 2016), biomagnetism (J. Li et al., 2010; Lin & Pan, 2009; Pan et al., 2005), tectonics (Jackson & Swanson-Hysell, 2012; S. Li et al., 2017; Van Hinsbergen et al., 2008), pollution monitoring (Muxworthy et al., 2001; C. Zhang et al., 2013), and extraterrestrial magnetism (Muxworthy et al., 2017; Tikoo et al., 2017), among many others. Despite this widespread usage, the analysis of hysteresis data can be nontrivial, and detrimental effects on the quality and accuracy of hysteresis data, such as off-center loops and drift are routinely unaccounted for (Jackson & Solheid, 2010).

Following a brief introduction to magnetic hysteresis, here we present some general guidelines for the improved measurement of magnetic hysteresis data and new graphical user interface software, *Hysteresis Loop analysis box* (*HystLab*), for the advanced processing and analysis of hysteresis loops. HystLab follows closely the recommendations proposed by von Dobeneck (1996) and, in particular, those of Jackson and Solheid (2010). In this introduction to HystLab, we briefly outline these procedures taking note of differences employed in our new software package.

Written in MATLAB, HystLab will run on all Windows, OS X, and Linux systems capable of running MATLAB v8 or above (no additional toolboxes are required). The HystLab package is available for download from https://github.com/greigpaterson/HystLab, and installation and operating instructions are given in the provided documentation.

## 2. The Basics of Magnetic Hysteresis

Measurement of a magnetic hysteresis loop begins by first saturating the magnetic moment ($M$) of a specimen in large positive (or negative) field ($B$). The intensity of the field is decreased to zero and increased in the

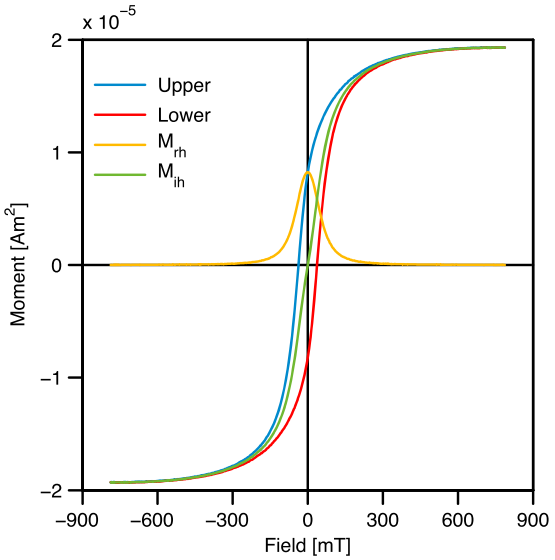


**Figure 1.** Example hysteresis loop. A basic hysteresis loop distinguishing the upper and lower branches as well as the remanent ($M_{rh}$) and induced ($M_{ih}$) hysteretic curves.

opposite direction to negative (or positive) saturation (blue branch in Figure 1). Finally, the field is swept back to positive (or negative) saturation to complete the loop (red branch in Figure 1). The sweep from positive to negative saturation is termed the upper branch and the sweep from negative to positive saturation is termed the lower branch (Figure 1). Under idealized conditions and for most specimens of natural material, the upper and lower branches are inverse (rotation) symmetric around the origin. That is, any point ($B_i$, $M_i$) on a loop can be inverted around the origin to ($-B_i$, $-M_i$), and lie exactly on the opposite branch. There are, of course, physical reasons why a hysteresis loop may not be centered and symmetric about the origin (e.g., Harrison et al., 2007; Housen et al., 1996), but for most geological materials it is reasonable to assume origin-centered symmetry, and deviations from symmetry can then be attributed to undesirable factors such as measurement noise, drift, and/or offsets.

Given the inverse symmetry expected for geological materials, when the lower branch of a noise-free hysteresis loop is inverted about the origin it will lie exactly on the upper branch. In practice, however, the match is rarely exact and the difference between the upper and inverted lower branch can be viewed as an estimate of the noise of a hysteresis measurement. This is the err(H) curve of Jackson and Solheid (2010), herein simply called the noise curve.

A basic hysteresis loop can be further processed into remanence and induced hysteretic curves (Rivas et al., 1981; von Dobeneck, 1996; Figure 1). The remanence hysteretic curve, $M_{rh}$, is half the difference between the upper and lower hysteresis branches, while the induced hysteretic curve, $M_{ih}$, is half the sum of the upper and lower hysteresis branches. Like a basic hysteresis loop, both $M_{rh}$ and $M_{ih}$ have expected symmetries: reflection symmetry about the vertical axis and rotation symmetry about the origin, respectively.

## 3. Measuring a Hysteresis Loop

Regardless of the sophistication of data processing and analysis, low-quality data will always yield low-quality results. In this section, we briefly outline some common artifacts in hysteresis loop data and simple approaches for improving the measurement quality of a hysteresis loop. These guidelines are particularly aimed at Princeton Measurements Corporation MicroMag 3900 vibrating sample magnetometers (VSMs; now owned by Lake Shore Cryotronics, Inc.) as these are the most widely used instruments in the rock magnetic community and are the ones with which we have most experience. Nevertheless, the basic ideas behind these recommendations are applicable to a wide range of equipment capable of measuring magnetic hysteresis loops. Similarly, many of these recommendations can be used to improve data for other measurements that can be performed on these types of instruments (e.g., isothermal remanent acquisition curves, or first-order reversal curves).

### 3.1. Improving Signal-to-Noise

Most VSMs have a number of settings that can be used to improve the signal-to-noise ratio (SNR) of a hysteresis loop. This includes the physical setup of the experiments such as the size of the specimen and the spacing between the sensing/pickup coils (pole gap), as well as software and measurement protocol settings such as the measurement average time, the field sweep mode, field stabilization time, and averaging multiple loops. The trade-off for measuring a higher-quality loop, however, is a longer measurement time per specimen, which may result in larger drift during measurement of a single loop.

One of the most obvious approaches to increase the moment signal of a hysteresis loop is to measure a larger specimen. For a specimen with uniformly concentrated magnetic particles, increasing the volume by a factor $n$ increases the magnetic moment by a factor $n$. A typical VSM specimen is a small cylindrical core or gel capsule specimen with a diameter of 4–5 mm and height of 5–6 mm (volume ≈ 0.125 $cm^3$). For weakly magnetized materials (e.g., carbonate sediment or chert), however, this size may not be sufficient to obtain data of sufficient quality for analysis. To produce a moment increase of a factor 10 requires increasing specimen

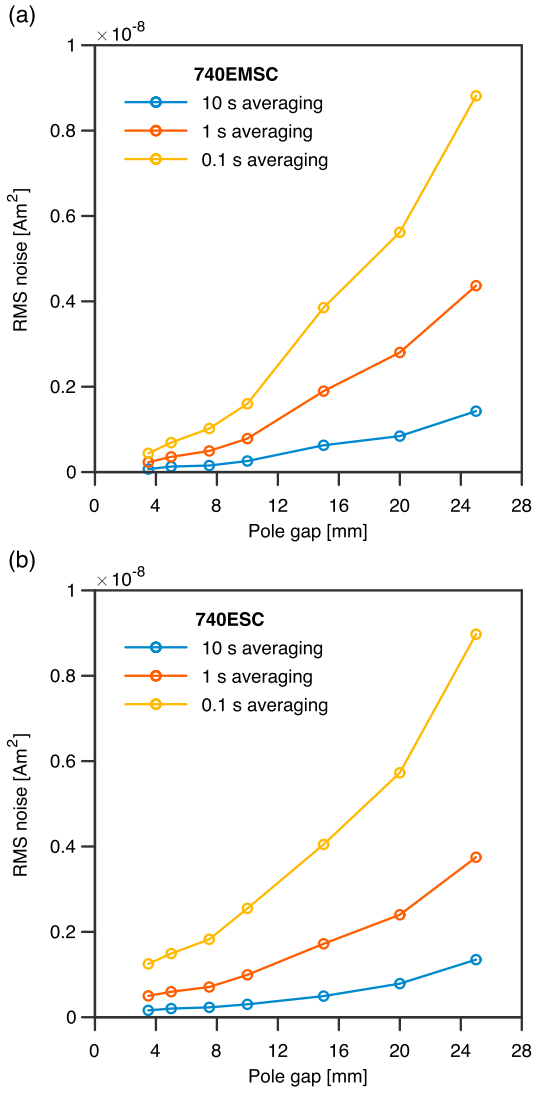


**Figure 2.** Moment root-mean-square (RMS) noise as a function of the gap between the pick-up coils of the Lake Shore 7400 series VSM when measured with different averaging times. (a) The 740EMSC VSM, which is optimized for small specimens. (b) The 740ESC VSM. Data are from Dodrill (2001).

dimensions by a factor of ~2.15 $\left(\sqrt[3]{10}\right)$ to a size of ~11 mm (volume ≈ 1.3 $cm^3$). A limiting factor with increasing specimen size is the specimen mass. A typical VSM has a mass limitation on the order of ~10 g and specimens that are heavier than this may introduce noise to the vibration system and, ultimately, can lead to failure of the vibration mechanism or damage the system and introduce a permanent and undesirable source of noise. For a typical lithified sediment with a density of ~2.2–2.8 $g/cm^3$, this mass restriction corresponds to a maximum volume of ~3.5–4.5 $cm^3$, or an equidimensional size of ~15–17 mm—a factor ~40–50 increase in moment compared to the typical 4- to 5-mm specimen. For powdered specimens, larger volumes can be used (lower-density material), or the powder can be more tightly compressed to increase the measurable mass, but packing too tightly may introduce unwanted magnetostatic interactions (Chen et al., 2005). A caveat to increasing specimen size is that this limits the minimum distance between the pickup coils used to measure the specimen moment—a larger specimen requires a large spacing, which reduces the overall moment sensitivity of the system.

Most VSM systems have adjustable spacing between the pickup coils used to detect the magnetic moment of a specimen, known as the pole or air gap. This adjustment not only allows for variable sizes of specimens to be measured but also offers higher moment sensitivity as well as higher applied fields for smaller pole gaps. Pole gaps can typically range from 3.5 mm to 25 mm, and although smaller and larger gaps are possible, they present problems in the form of physical interference with specimen holders and practical limits on moment sensitivity, respectively. In Figure 2 we replot moment root-mean-square (RMS) noise as a function of pole gap spacing for the Lake Shore 7400 series VSMs (Dodrill, 2001). Increasing the pole gap from ~7 to 8 mm (the minimum gap suitable for a 4- to 5-mm specimen) to ~14 mm to accommodate a 10 times increase in volume would result in a 2–4 times increase in the moment noise, irrespective of the measurement averaging time. Although this source of noise can vary from system to system, increasing the size of the specimen can yield a stronger signal without an overly large loss of moment sensitivity due to a wider pole gap.

As a general rule of thumb, ~5 mm chips or cores are sufficient for most volcanic materials and ~10 mm diameter gel caps (~1.4 $cm^3$) hold enough material to measure many powdered sediments. For weaker materials, 4 $cm^3$ (~16 mm diameter) paleomagnetic cubes can be used. These are smaller than typical paleomagnetic cubes (8 $cm^3$) but allow the maximum possible material volume while not overloading the VSM drive system. In some cases, however, measuring a larger specimen may be not possible (e.g., insufficient material) and other methods of noise reduction may be needed.

An alternative way to improve hysteresis signal to noise is to increase the measurement averaging time, which is the duration over which each moment measurement is averaged. The MicroMag 3900 VSM has a sampling rate of one measurement per 10 ms and is capable of averaging over times of 10 ms to 10,000 s (averaging 1 to $10^6$ measurements). In general, however, averaging times less than 1 s, most commonly less than 500 ms, are sufficient for measuring a hysteresis loop on a typical geological material. In Figure 3a we show a hysteresis loop measured in continuous field sweep mode (described below) with an averaging time of 100 ms, and in Figure 3b we show the same specimen measured in continuous mode with a 200 ms averaging time. By doubling the averaging time, we reduce the RMS noise curve by a factor of 1.66 (~√2). Thirty replicates of these measurements confirm the √2 reduction in the average noise (average RMS noise ratio of 1.51), which is expected if measurement noise is approximately independent and identically distributed Gaussian noise. This level of noise reduction is a general feature of increasing averaging time, such that

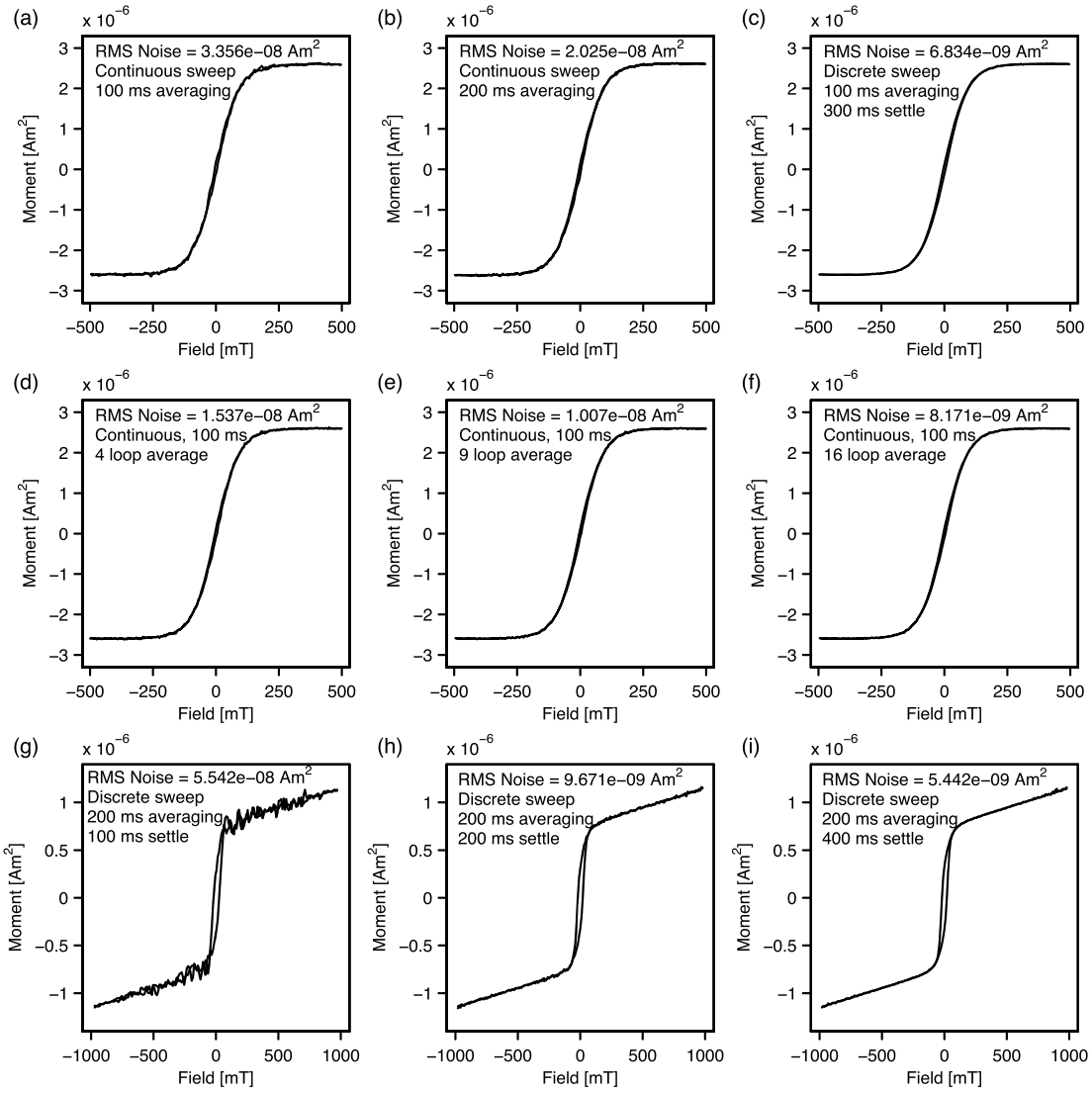


**Figure 3.** Examples of hysteresis loops with differing measurement parameters and the resultant noise levels. Hysteresis loops from (a) volcanic speck (<1 mg) measured with a continuous field sweep with a 100 ms averaging time and (b) a 200 ms averaging time. The hysteresis loops measured using a discrete field sweep with a 300 ms settling time before measuring with a 100 ms averaging time. The average of (d) 4, (e) 9, and (f) 16 loops measured in continuous mode with 100 ms averaging. A cultured magnetotactic bacteria specimen (J. Li et al., 2012) measured in discrete mode with 200 ms averaging time and (g) 100 ms, (h) 200 ms, and (i) 400 ms settling time.

increasing the averaging time by a factor $n$ corresponds to $\sim\sqrt{n}$ reduction in noise, but increasing measurement time by a factor $n$. The slightly higher level of noise reduction we observe (1.51 versus 1.44) is likely a consequence of smoothing introduced during necessary interpolation of the hysteresis loop data (see section 4).

Another measurement setting that can be adjusted is the field sweep mode, which offers two possible options: continuous or discrete. Using continuous sweep mode, the field is swept over the measurement averaging time and the average field and moment are recorded. In discrete mode (also known as point-by-point mode), the field sweep is paused for a specified time (called the pause or settling time) to allow the field to stabilize before the measurement proceeds. Continuous mode offers a rapid measurement option that works well for strong specimens or where the field sweep rate is low. For weaker samples, discrete mode often offers a higher signal to noise, but with a longer measurement time. In Figure 3c, we show an example of a loop measured in discrete mode with an averaging time of 100 ms and a settling time of 300 ms (i.e., the field is paused for 300 ms before the field and moment are averaged over the proceeding 100 ms). Compared

with the equivalent loop measured in continuous mode (Figure 3a), we see a reduction of noise by a factor of 4.9 (30 replicates yield an average RMS noise reduction by a factor ~5), but with a factor ~4.6 increase in measurement time. For weak specimens, measurement in discrete mode often offers a better trade-off between improved signal to noise and increased measurement time (factor ~$n$ increase in time yields a factor ~$n$ decrease in noise) than simply increasing the averaging time (factor ~$n$ increase in time yields a factor ~$\sqrt{n}$ decrease in noise). The magnitude of noise reduction switching from continuous to discrete field sweep depends not only on the choice of averaging and settling times but also on the exact shape of the loop—hysteresis loops with large gradient changes will benefit more from discrete sweep measurements.

Another approach to improving SNR is to average multiple hysteresis loops. To do this, it is often, but not always, necessary to correct for measurement drift between each loop before averaging (for our example data it is necessary and the drift is described in section 3.2). After correcting for interloop drift, we take the specimen shown in Figure 3a and average it with a total of 4, 9, and 16 loops (Figures 3d–3f). This averaging requires interpolation of all loop moments onto the same field spacing as the loop in Figure 3a. Although this interpolation adds a degree of smoothing, the noise reduction by averaging $n$ loops broadly follows the expected ~$\sqrt{n}$ factor reduction (noise is reduced by a factor 2.2, 3.3, and 4.1, for averaging 4, 9, and 16 loops, respectively). Like increasing the averaging time, averaging $n$ loops comes with a factor $n$ increase in the total measurement time. It should be noted, however, that to measure these 16 loops in continuous sweep mode with 100 ms averaging, took approximately 720 s (with 402 points per loop). A similar or slightly lower noise can be achieved by using the discrete sweep mode with 100 ms averaging and 300 ms settling time, which requires just a single loop measurement time of only ~210 s (compare Figures 3c and 3f). Again, measuring in discrete mode often offers a better trade-off between improved signal to noise and increased measurement time.

When measuring in discrete mode, the field settling time offers another means of reducing measurement noise. In Figures 3g–3i, we compare three loops measured in discrete mode with an averaging time of 200 ms and settling times of 100, 200, and 400 ms. We observe that a factor $n$ increase in settling time results in a factor ~$n^2$ reduction in the loop RMS noise (confirmed by additional measurements at 100 and 300 ms averaging). This large reduction in noise rapidly approaches the manufacturer's nominal moment sensitivity of ~$0.5 \times 10^{-9}$ $Am^2$ (1,000 ms averaging, pole gap unspecified), and in our collective experience, settling times of $>$500 ms offer little improvement at the expense of considerably longer measurement times. Generally, settling times of 100–300 ms are sufficient for most measurements.

Overall, for weak and noisy hysteresis loops, measuring in discrete field sweep mode with averaging times of 100–300 ms and settling times of ~300 ms offers the best balance between maximizing signal-to-noise, while maintaining a reasonable measurement time (hence minimizing drift). Each specimen and instrument is, of course, unique, and each measurement should be tailored appropriately. For example, chips of volcanic materials that are $>$ ~2–3 mm in size are typically strong enough to be measured in continuous mode with short (~100 ms) averaging times—the example in Figure 1 is a such a chip but has a RMS noise of ~$1 \times 10^{-8}$ $Am^2$, or $<$0.05% of the saturation moment ($M_s$), while the example in Figure 3a has a RMS noise of ~1.3% of $M_s$. The above descriptions of loop noise and guidelines for reduction should serve as general starting point for the majority of specimens encountered by the rock and paleomagnetic community.

### 3.2. Minimizing Drift

Although the sources of drift can be difficult to characterize and quantify, many can be related to temperature or mechanical effects. Thermal factors are relevant not only to the temperature of the specimens being measured, but also to the ambient temperature of the room and to temperature changes of the experimental apparatus as the experiments proceed. Mechanical factors can be related to the solidity/friability of the specimen, specimen position during measurement, or the physical mechanisms and electronics of the instrument being used.

Temperature changes in the specimen being measured are one potential source of thermal drift. Not only can this affect measurement of the temperature dependence of magnetic properties, but can also have an impact on measurements at room temperature due to the temperature between the pole pieces being influenced by the temperature of the magnets. This type of thermal drift can strongly influence specimens with large paramagnetic components such as sediment samples and is most likely the main cause of extreme drift and failure of loops close after return to the initial saturation field.

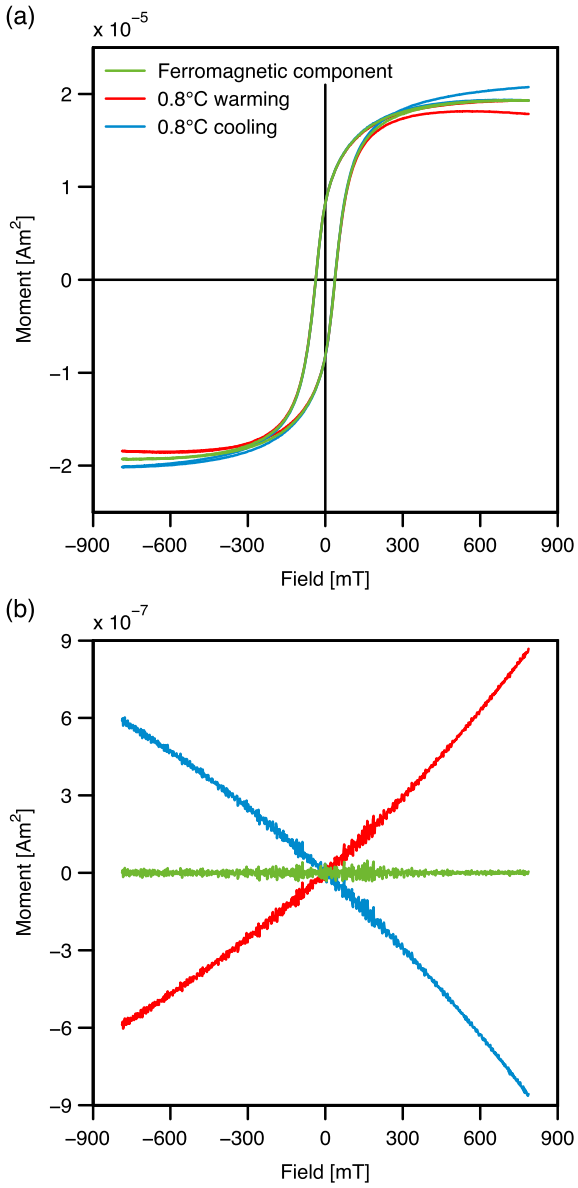


**Figure 4.** Theoretical model of paramagnetic thermal drift. (a) Example hysteresis loops of a theoretical ferromagnetic component mixed with a strong paramagnetic component that experiences thermal drift during measurement. The green loop is the expected loop if the specimen experiences no temperature change during measurement. The red and blue loops are for a specimen that experiences warming and cooling toward ambient temperature, respectively, during measurement. All loops have been corrected for the known high-field paramagnetic susceptibility. (b) The resultant noise curves. Colors are the same as in panel (a).

This type of thermal drift, which we term paramagnetic drift, can be described by a simple temperature model of paramagnetic moments (Jackson & Solheid, 2010). Curie's Law states that the paramagnetic magnetization ($M_p$) in an applied field, $B$, is inversely proportional to temperature, $T$:

$$M_p(B,T) = \frac{CB}{\mu_0 T}, \tag{1}$$

where $C$ is the Curie constant and $\mu_0$ is the permeability of free space. If the temperature of a specimen changes from an initial temperature of $T_0$ to temperature $T_i$, the paramagnetic magnetization at $T_i$ can be expressed as

$$M_p(B,T_i) = M_p(B,T_0)\frac{T_0}{T_i}. \tag{2}$$

Typically, a specimen will be at equilibrium with the temperature of room where it was stored before measurement. However, because of the balance between heat generated by the magnets and heat dissipated by the magnet cooling system, the temperature between the VSM pole pieces can often be different from the general room temperature. Therefore, when a specimen is measured, it may be out of thermal equilibrium with the measurement space. In such a scenario, the change of a specimen's temperature follows Newton's Law of Cooling:

$$T_i = T(t_i) = T_A + (T_0 - T_A)\exp(-kt_i). \tag{3}$$

where $T_A$ is the ambient temperature (temperature between the VSM pole pieces), $k$ is a rate constant, and $t_i$ is the time of the $i$th measurement.

In Figure 4 we show examples of hysteresis loops that experience drift due to a change in temperature inducing a change in paramagnetic magnetization. Here we take the ferromagnetic loop shown in Figure 1 and add in a paramagnetic contribution such that in a 1 T field the ratio of paramagnetic to ferromagnetic magnetization ($M_p/M_f$) is 35 (many natural sediments have ratios of ~1 to >50). The initial specimen temperature is set to 20 °C and we model two loops where the ambient temperature is initially 1.5 °C above and below the specimen temperature, such that the specimen experiences warming and cooling, respectively. All loops, therefore, start at the same point (Figure 4). The rate constant in equation (3) is set such that the specimen does not reach thermal equilibrium, but experiences a 0.8 °C temperature change over the measurement of each loop. All loops have been corrected for the paramagnetic contribution using the known high-field paramagnetic susceptibility.

The green loop in Figure 4a is the loop that would be measured if there is no change in the specimen temperature (i.e., specimen and ambient temperatures are the same). If the ambient temperature is intially above specimen temperature, then the specimen experiences warming toward ambient and the loop fails to close after returning to positive saturation with the lower branch lying well below the upper branch (red loop Figure 4a). The apparent $M_s$ value after high-field slope correction is lower than the true value. If the specimen is intially above ambient temperature and experiences cooling toward ambient, the lower branch crosses the upper as the loop returns to positive saturation and ends well above the upper branch (blue loop Figure 4a). The apparent $M_s$ value, however, is higher than the true value. This lack of closure can be quantified by a closure error ($M_{ce}$), which is the difference between the moments of initial and final peak positive field measurements. In both cases $M_{ce}$ is ~7.5% of the true $M_s$ value.

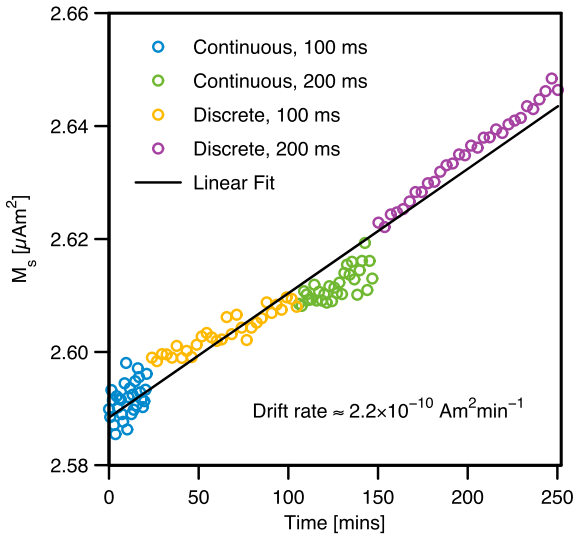


**Figure 5.** Moment drift caused by specimen movement over time. Change in saturation moment over the ~250 min needed to measure the 120 loops comparing averaging times and continuous and discrete field sweep modes.

This type of drift always manifests as failure of the loop to close (Figure 4a) and a nonlinear noise curve (Figure 4b). These features, however, can be variable as they are dependent not only on the relative strength/abundance of paramagnetic minerals with respect to the ferromagnetic/ferrimagnetic contribution, but also on the initial temperature of the specimen, ambient temperature, as well as the thermal properties of the specimen, which control $k$ in equation (3).

This kind of thermal drift can be minimized by a number of simple steps to control temperature fluctuations. Among other measures, this can include regulating room temperature with the use of air conditioning, ensuring laboratory doors are closed to prevent uneven temperatures, shading windows to avoid heating by sun glare, and minimizing the temperature difference between room temperature and the water used to cool the electromagnets (but maintaining appropriate operating temperature). Similarly, allowing a specimen to thermally stabilize before measurement will reduce drift, particularly if temperature-dependent hysteresis loops are being measured. Even for room temperature measurements this effect can be important if the cooling-water temperature and temperature in the magnet air gap differ significantly from the general room temperature. In such cases it is beneficial to allow the samples to thermally equilibrate on the electromagnet base prior to measurement. As noted before, thermal drift has the strongest influence on specimens that have large paramagnetic contributions with respect to the ferromagnetic component. So, these precautions may not be needed for all types of specimens.

Drift can also be caused by nonthermal mechanisms. This can include instabilities in the vibration system, electronic drift, or physical movement of the specimen during measurement. Quantifying the manifestation of these types of drift is difficult and, depending on the source, may be a linear or nonlinear function of time and/or field. Avoiding extremely heavy specimens, ≥10 g, which are at or beyond the specifications of the VSM system being used, can minimize vibrational drift and prevent long-term damage. Physical movement of the specimen during measurement can occur if it is not properly attached to the holder or if a powder is not properly compacted.

For the 30 replicates of each loop shown in Figures 3a–3c (plus 30 replicates of the loop measured in discrete mode with 200 ms averaging and 300 ms settling time; a total of 120 loops), the total measurement time for these 120 loops was ~250 min. Over this time, we observe an approximately linear increase in $M_s$ of ~$6.3 \times 10^{-8}$ Am$^2$ (~2.4% of the average $M_s$ value), which corresponds to a drift rate of ~$2.2 \times 10^{-10}$ Am$^2$/min (Figure 5). Drift for the longest individual loop measurements of ~210 s (discrete field sweep with 200 ms averaging) is on the order of 0.02% of $M_s$ and can be neglected. This specimen was a speck of basalt (<1 mg) mounted to the VSM sample holder using silicon grease and although this drift is small, this is an example of mechanical drift related to changes in the specimen's position during measurement. Such movement can be avoided by properly fixing the specimen to the holder.

For solid specimens, glue can be easily used to affix the specimen to the holder, but allow sufficient time for the glue to dry; otherwise, the specimen may fall off during measurement. We recommend the use of water-based polyvinyl acetate glue (superglue can easily damage friable specimens and is harder to remove from the holder). For powdered specimens packed into gel caps or cubes, an additional top layer of cotton wool can help better compact the specimen and avoid particle movement. In extreme cases, the powder can be impregnated with glue to solidly bind the particles, but this is generally not needed.

### 3.3. Other Influences

Instruments for measuring hysteresis loops typically have nominal moment ranges of ~$10^{-11}$–1 Am$^2$ and specimens weaker or stronger than this cannot be easily measured. For a MicroMag 3900 VSM (nominal moment range of $5 \times 10^{-8}$ to $1 \times 10^{-2}$ Am$^2$), the moment range (sensitivity setting) has to be selected manually. The VSM software warns if the range is set too low for the specimen moment, but if missed, incorrect moment range can have a detrimental impact on the loop measurement. This can easily happen if the

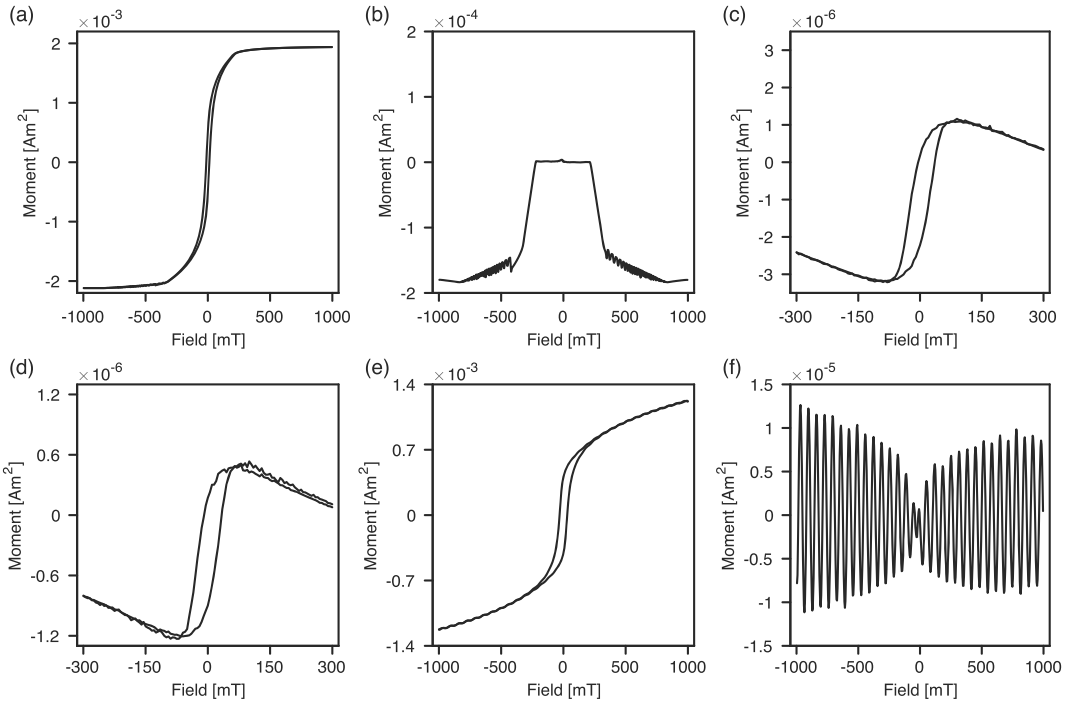


**Figure 6.** Examples of hysteresis loops suffering from other detrimental effects. (a) A hysteresis loop measured with the moment range set too low. (b) The noise curve of the loop shown in panel (a). (c) A hysteresis loop offset from the plot origin due to the presence of an electrostatic charge on the specimen holder. (d) A specimen with an electrostatic charge that partially dissipated during measurement. (e) A hysteresis loop that suffers from vibrational instability. (f) The noise curve of the loop shown in panel (e) reveals a clear periodicity to the noise. The loop in panels (e) and (f) is a volcanic chip from Muxworthy et al. (2011).

high-field slope is negative and the peak moment occurs at low fields (cf. Figure 6c), or when the loops are measured as a function of temperature and the specimen moment increases beyond the initially set range. Figure 6a is an example of a loop measured with the moment range set too low. The high-field branches have a distinct change in slope that does not follow the natural curvature of the loop. For other specimens, this effect may occur subtly at higher fields and may give the impression of reaching saturation. The noise curve (Figure 6b) has a distinct plateau shape that is characteristic of the moment range being too low and can be diagnostic when the effects are subtle.

Some systems are capable of dynamically adjusting the moment range and such artifacts are not an issue. Where the range has to be set manually, the range should be set prior to measurement with the specimen in place and most commonly with the peak measurement field applied. In some cases, however, if the specimen has a strong diamagnetic component and a negative high-field slope, the maximum moment in the loop measurement occurs at lower fields and a large portion of the loop will need to be measured before an incorrect moment range is detected. Data with the moment range set too low must be remeasured to obtain interpretable data.

Most VSMs will allow the vibration amplitude to be adjusted. Reducing the vibration amplitude reduces the magnitude of the voltage induced in the pickup coils and allows the moment sensitivity to be adjusted to a higher range. If the moment range is set to the instrument maximum and this effect still occurs, the specimen is too strong and should be reduced in size then remeasured. Alternatively, if reducing sample size is undesirable, a wider pole gap may allow measurement (a wider pole-gap reduces the magnitude of the voltage induced in the pickup coils; note that the system should be recalibrated if the gap is adjusted).

In Figure 6c we show an example of a hysteresis loop from a magnetotactic bacteria (MTB) specimen deposited in a plastic cube (Paterson et al., 2013). The loop is offset from the plot origin due to an electrostatic charge on the plastic cube. Such oscillating electrostatic charges are equivalent to time-varying currents, which generate changing magnetic fluxes that are additive to that from the specimen moment, and

typically manifest as a large moment offset with negligible field offset. The electrostatic signal is independent of applied field, which preserves the size and shape of the loop and allows for correction of the offset (see section 4.2).

Figure 6d is a hysteresis loop from another MTB specimen in a plastic cube with an electrostatic charge. In this example, the static charge partially dissipates during measurement causing the lower branch to lie above upper branch on returning to positive saturation. The various methods used to correct for loop drift (outlined in section 4.4) perform poorly for this type of drift and such loops are best remeasured (the distribution of moment drift depends on when and how fast the charge dissipates). Anti-static sprays can help dissipate electrostatic fields before measurement. In laboratories where electrostatic charges are a long-term problem (e.g., locations with seasonal periods of low humidity), air ionizers can be used to reduce the buildup of static charges.

On VSMs, the vibration drive system can also be a source of noise. Figure 6e is an example of loop that suffers from vibrational drive instability. Examination of the noise curve (Figure 6f) reveals that the noise is highly periodic, and a spectral analysis (not shown) indicates significant power at an angular frequency of 1.84 Hz, confirming that this is not random noise. The exact cause of this periodic noise is unknown, but is likely due to instability in the electronic feedback loop that controls the vibration drive system (H. Reichard, personal communication, 2018). Although observable, in this case, the magnitude of the instability is insufficient to greatly affect the interpretation of the loop statistics.

Other possible sources of vibrational drive instability include insecure drive rods, loose specimen holders or specimens not being fully secured to the holder, the specimen touching the pole pieces or Hall probe, or noise introduced by overloading the system with heavy ($>$10 g) specimens. For mechanical sources of instability, simple fixes of securing drive rods and specimens, and ensuring that vibrations are unimpeded will resolve any noise issues. Particular attention should be paid to ensure the specimen does not physically interact with Hall probe as this may damage the probe. For the case of periodic instability (Figures 6e and 6f), restarting the instrument, reseating the vibration drive system cables, and adjusting the orientation stage have been known to resolve this issue. If these simple approaches fail to remove vibrational drive instability, users should consult the instrument manufacturers for further advice.

## 4. Hysteresis Processing

Following measurement of a hysteresis loop, it is necessary to process the data appropriately to correct for unavoidable negative influences (e.g., unavoidable drift) and isolate the desired components before extracting the parameters and statistics of interest for further analysis. To that end, we have developed new graphical software called HystLab to aid the paleomagnetic and rock magnetic community in processing and analyzing hysteresis loop data. The remainder of this paper will discuss the functionality of HystLab and the tools available to minimize the detrimental impact of measurement artifacts on the final interpretation of hysteresis data.

HystLab supports a number of advanced processing options that are combined with automated decision processes used by default for all specimens when they are first loaded. This includes automatic centering of hysteresis loops and automatic decisions on drift and saturation slope corrections (details outlined below). In general, this default processing performs well for most geological specimens and provides a quick starting point for users to analyze their data. The default processing, however, may not be suitable for every specimen. We therefore strongly encourage analysts to carefully consider the processing of each specimen to ensure appropriateness.

### 4.1. Loop Interpolation

All hysteresis processing in HystLab is based around the assumed symmetry of the basic hysteresis loop and the remanence and induced hysteretic curves. When comparing the upper and lower branches it is necessary to interpolate to consistent field steps. When a raw hysteresis loop is initially processed and analyzed, the lower branch is inverted and linearly interpolated to the field steps of the upper branch. For all other processing, both the upper and lower branches are linearly interpolated on to a regularly spaced field grid. To avoid extrapolation of data where there are no measurements, the peak field of the grid is taken as the lowest of the four absolute peak fields (termed $B_{max}$). To avoid artificially oversampling the loop, the number of points

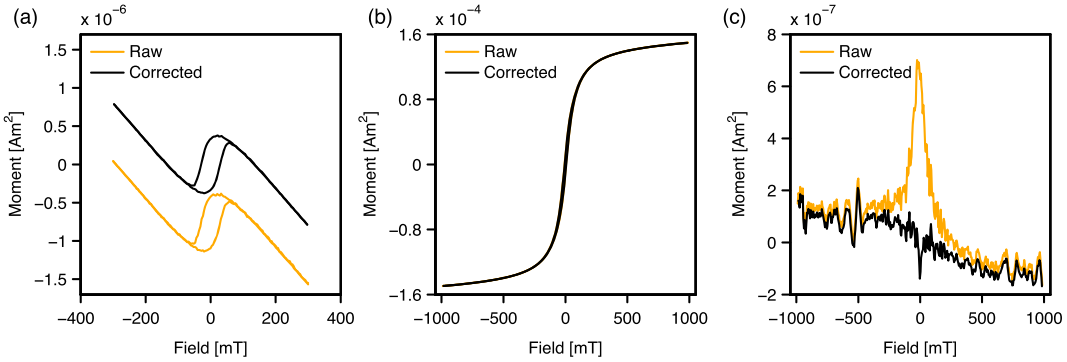


**Figure 7.** Examples of specimens requiring loop centering. (a) A magnetotactic bacteria specimen with visually obvious loop offset (Paterson et al., 2013). (b) A volcanic specimen (Paterson et al., 2010) with more subtle offset, which is evident as a zero-field spike in the noise curve (c) that is removed after loop centering. RMS noise is $3.679 \times 10^{-6}$ $Am^2$ before correction and $1.907 \times 10^{-6}$ $Am^2$ after.

used, $n$, is taken to be the minimum number of points used to measure either the upper or lower branches (after fields with absolute field values $< B_{max}$ are removed). The interpolation field grid is $n$ equally spaced field points in the range $[B_{max}, -B_{max}]$. These necessary interpolations inevitably introduce a degree of data smoothing and as a result, estimates of noise and loop quality statistics (described below) are likely to be slight underestimates and overestimates, respectively, of their true values.

### 4.2. Loop Centering

If uncorrected, asymmetry of a loop about the origin may lead to misestimating of hysteresis descriptive statistics (e.g., $M_s$, $M_{rs}$, $B_c$). In Figure 7a we show an example of extreme loop offset of a MTB specimen with a strong diamagnetic signal from the specimen holder (Paterson et al., 2013). This large moment offset (on the order of the specimen's $M_s$) is likely caused by an electrostatic charge on the specimen's plastic holder. A subtler example of loop offset is seen from a volcanic specimen from Paterson et al. (2010; Figure 7b). This less visually obvious offset becomes evident in the noise curve where it manifests as a distinct peak around zero field (Figure 7c). This peak is removed and the root-mean-square noise level is reduced by a factor 2 after correctly centering the hysteresis loop (Figure 7c). Following loop centering, a systematic trend in the noise curve becomes more evident (Figure 7c)—this is due to measurement drift (drift corrections are discussed in section 4.4).

Loop offset is corrected for following Jackson and Solheid (2010), whereby the offset along the field axis is found by maximizing the linear correlation between upper branch and inverted lower branch when the lower branch is shifted by the correct field offset ($B_0$). The intercept of a linear model fit to the $B_0$ shifted lower branch and upper branch corresponds to twice the offset along the moment axis ($M_0$).

In HystLab, a Nelder–-Mead optimization routine (Lagarias et al., 1998) is used to find the correct field offset. For determining the moment offset, we employ a major axis regression model, which, given the lack of obvious choice of dependent and independent variables (upper versus lower branch moments) and the likely similar noise structure of the upper and inverted lower branches, is more appropriate than a standard linear regression model.

### 4.3. Loop Quality

The squared linear correlation ($R^2$) between the upper and inverted lower branches can be used to define a quantitative measure of the quality ($Q$) of a hysteresis loop (Jackson & Solheid, 2010). The definition of $Q$ used in HystLab is given by

$$Q = \log_{10}\left(\frac{1}{\sqrt{1-R^2}}\right), \tag{4}$$

This differs from the definition of Jackson and Solheid (2010) who erroneously omitted the square root in the denominator in their paper; although it was included in their calculations and internal software at the

Institute for Rock Magnetism, University of Minnesota, which has been used to quantify numerous hysteresis loops. $Q$ values in HystLab take the square root to maintain consistency, and we view the above definition of $Q$ as correcting that of Jackson and Solheid (2010).

In addition to the quality of the raw loop ($Q$) and the fully processed loop ($Q_f$), HystLab also determines the quality of the remanent ($Q_{rh}$) and induced ($Q_{ih}$) hysteretic curves. These $Q$ values are based on the expected reflection and rotational symmetries of the remanent and induced curves, respectively, and the correlations between the negative and positive field halves.

### 4.4. Drift Correction

Given the diverse possible sources of hysteresis loop drift, a number of different approaches to drift correction have been proposed and HystLab supports many of these. In addition to the option of applying no drift correction, HystLab offers four types of correction: (1) positive field correction, (2) upper branch correction, (3) symmetric averaging, and (4) paramagnetic drift correction. The positive field correction subtracts the smoothed noise curve from the positive field segments of the hysteresis loops: The positive field half of the noise is subtracted from the positive field half of the upper branch and the negative field half of the noise curve (reflected to positive fields) is subtracted from positive field half of the lower branch (Jackson & Solheid, 2010). The upper branch correction subtracts the smoothed noise curve from the upper branch of the hysteresis loop only (Jackson & Solheid, 2010). Symmetric averaging follows von Dobeneck (1996), whereby the upper and inverted lower branches are averaged and vertically shifted by half their tip-to-tip separation to ensure loop closure; This results in a zero noise curve. The paramagnetic drift correction accounts for changes in paramagnetic moment due to changes in specimen temperature and is described in detail below.

An automatic correction option is available, which decides between positive field and upper branch corrections. The decision is based on the ratio of drift in the high-field range (≥75% of the peak field) to the low-field range. If drift tends to occur in the high-field range, then the positive field correction is applied; otherwise, the upper branch correction is applied. In most cases, the positive field correction tends to perform best and is therefore favored in the automatic correction approach. We note, however, that although these methods for drift correction generally recover many statistics with reasonable accuracy, the detailed shape of the loop may not always be accurately recovered for certain types of drift (e.g., paramagnetic thermal drift).

The paramagnetic drift correction is newly introduced here and is based on the thermal model of paramagnetic drift described in section 3.2, which after expansion, describes the change in paramagnetic moment in terms of the ratio ($T_r$) of a specimen's initial absolute temperature ($T_0$) to ambient absolute temperature in the measurement space ($T_A$): $T_r = T_0/T_A$. The first step of this method is to correct drift using the positive field correction described above, and the user-defined high-field slope correction (see section 4.5) is applied to estimate the high-field/paramagnetic susceptibility ($\chi_{HF}$). If no saturation slope correction is applied a linear fit is made to the data at fields ≥70% of the peak field (this slope correction is not applied to the final loop, but used only to estimate $\chi_{HF}$). This estimate of $\chi_{HF}$ is used to estimate the paramagnetic magnetization ($M_P = \chi_{HF}\mu_0 B$). The thermal rate constant, $k$, and the relative temperature ratio $T_r$ are then optimized to fit the observed noise curve. Each point of the hysteresis loop is then corrected for the predicted change in the paramagnetic moment. Following this, the above described automatic drift correction routine is used to apply either a positive field or upper branch correction to account for any other drift not related to paramagnetic thermal instabilities.

An advantage of this correction over others is that it provides a justifiable means of distributing components of drift across all measurements and not just across a restricted range of data (e.g., positive fields only). Furthermore, for specimens that experience this type of thermal drift, the hysteresis loop shape is generally better recovered than with the other corrections.

An example of a specimen with extreme paramagnetic drift is shown in Figure 8a. This specimen is a relatively weak lake sediment with a ferromagnetic component dominated by detrital magnetite (Liu et al., 2015). This specimen is strongly paramagnetic with a 1 T para-to-ferromagnetic magnetization ratio ($M_P/M_f$) of ~35 (cf. the theoretical example in section 3.2). After linear high-field slope correction, the lower branch crosses the upper branch and lies well above the upper branch resulting in a closure error of $M_{ce} = -1.993 \times 10^{-7}$ Am$^2$ (~65% of the estimated $M_s$). The noise curve is nonlinear with an RMS of $5.570 \times 10^{-8}$ Am$^2$ or ~18% of $M_s$ (Figure 8b). A positive field drift correction reduces the closure error ($M_{ce} = -6.390 \times 10^{-10}$ Am$^2$;

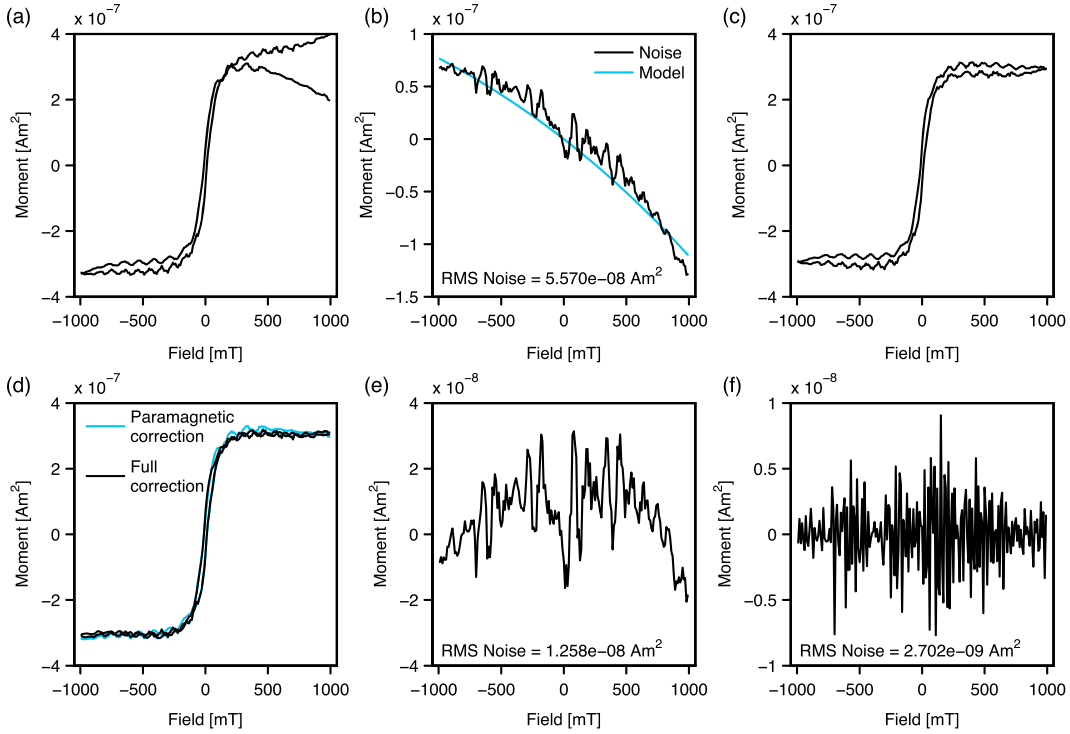


**Figure 8.** Example of hysteresis loop drift and the paramagnetic drift correction. (a) A weak lake sediment sample from Liu et al. (2015) where the loop fails to close after returning to positive saturation. (b) The noise curve (black line) exhibits a clear nonlinear field-dependent trend indicative of drift. This trend can be well modeled by a paramagnetic thermal drift model (blue line). (c) The hysteresis loop closes after positive field drift correction, but the overall shape of the high-field regions is not satisfactory and does not match the geological context of the specimen. (d) The hysteresis loop after paramagnetic drift correction only (blue loop) and after applying the combined paramagnetic and positive field drift correction (black loop). (e) After paramagnetic drift correction the root-mean-square (RMS) noise is reduced, but considerable structure remains in the noise curve, indicating other drift sources are present. (f) The noise curve is flat after the full drift correction.

~0.2% of $M_s$), yields more acceptable saturation behavior, and reduces the RMS noise ($2.783 \times 10^{-9}$ Am$^2$, ~1% of $M_s$). Although this loop looks more reasonable, the high-field portions are offset from each other and close only at the peak fields, giving the impression of high coercivity lobes (Figure 8c). The shape factor (Fabian, 2003) of the loop is 1.47. This is indicative of extremely wasp-waited behavior and the presence of a high-coercivity component, which is not seen in isothermal remanent magnetization acquisition data and does not fit with the geological context of the specimen (Liu et al., 2015, 2016). An upper branch correction fails to reduce the loop closure error and symmetric averaging exaggerates the high-coercivity lobes yielding a loop shape factor of 1.67.

The paramagnetic drift model fit to the noise curve is shown in Figure 8b and the paramagnetic drift corrected loop in Figure 8d. The loop is considerably more closed than before correction (postcorrection $M_{ce} = -1.340 \times 10^{-8}$ Am$^2$) and the high-coercivity lobes seen in positive field corrected loop are absent. Although after applying only the paramagnetic drift correction RMS noise is reduced ($1.258 \times 10^{-8}$ Am$^2$), considerable structure remains in the noise curve, which indicates that not all drift has been corrected for and another source of drift is likely present (Figure 8e). After applying the paramagnetic drift correction followed by the upper branch correction, the RMS is further reduced and becomes flat, which should be expected from random measurement noise. The fully corrected loop (Figure 8d) changes only slightly, but both RMS noise ($2.702 \times 10^{-9}$ Am$^2$) and the closure error are reduced ($M_{ce} = -6.700 \times 10^{-9}$ Am$^2$), yielding a much more reasonable hysteresis loop that can be more easily interpreted. The shape factor for the fully corrected loop, 0.06, indicates a constrained coercivity population, which is more consistent with the geological context of the specimen (Liu et al., 2015, 2016).

The paramagnetic thermal drift model estimates a temperature ratio of 1.036 for this hysteresis loop. At the Institute of Geology and Geophysics, Chinese Academy of Sciences, where this measurement was performed, the VSM electromagnets are cooled with chilled water running at ~17–19 °C, which would yield an initial

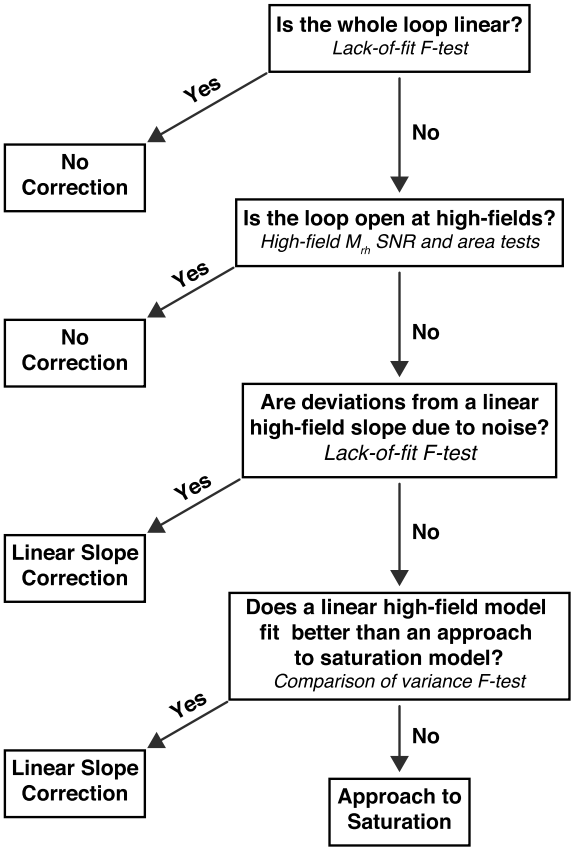


**Figure 9.** Schematic of the decision process when applying an automated high-field slope correction.

specimen temperature of ~27–29 °C. Although high for the time of measurement (mid-May with typical daytime ambient temperatures on the order of ~20–26 °C), it is still plausible. The exact room and specimen temperatures were not measured, so we cannot exclude the possibility of unusual temperature conditions such as sun glare warming, which can occur. Similarly, we cannot exclude the possibility that the model may be fitting other components of drift not related to paramagnetic thermal effects and this may skew the estimated temperature ratio.

This paramagnetic drift correction is not suitable for all specimens and works best for those with a distinct lack of loop closure and strongly nonlinear noise curve (e.g., Figures 8a and 8b). For example, applying this correction to the loop shown in Figure 7b (noise curve is given in Figure 7c) yields a temperature ratio of ~1.19. That is, the initial temperature of the specimen was ~20% higher than ambient. For an ambient temperature of ~293 K (~20 °C) this estimates a specimen temperature of almost 80 °C, which is physically unreasonable and indicates that the drift is unlikely to be related to paramagnetic thermal effects. When applying this type of drift correction these factors should always be considered when assessing the physical plausibility of the model and correction.

### 4.5. Saturation Slope Correction

In sufficiently high magnetic fields, the moment of ferromagnetic and ferrimagnetic materials saturates, while the moments of paramagnetic and diamagnetic materials continually increase or decrease, respectively. Therefore, when exploring the remanence capability of complex natural samples that are a mixture of magnetic carriers, it is necessary to correct the high-field portion for nonsaturating components. HystLab supports two standard approaches: a linear high-field slope correction and an approach to saturation correction (Fabian, 2006; Jackson & Solheid, 2010).

The linear correction assumes that the high-field portion of the ferromagnetic component is saturated and fits a linear model to the high-field data to correct the slope by removing the antiferromagnetic, paramagnetic, and diamagnetic contributions (i.e., nonsaturated components). The approach to saturation correction assumes that the high-field portion of the ferromagnetic component is not yet fully saturated, but is in the reversible regime approaching saturation. This method fits the high-field data with a model of the form:

$$M(B) = \chi_{HF}B + M_s + \alpha B^{\beta}, \tag{5}$$

where $\chi_{HF}$ is the high-field susceptibility, $M_s$ is the saturation moment, and $\alpha$ and $\beta$ are approach to saturation coefficients (Fabian, 2006; Jackson & Solheid, 2010). The approach to saturation model is fitted similarly to the method outlined by Jackson and Solheid (2010), whereby 100 β values evenly distributed on the interval $[-2, -1]$ are specified and equation (5) is solved to determine the remaining coefficients and the model that best fits the data.

HystLab includes an automated slope correction routine that tests if a high-field slope correction should be applied and then tests the appropriateness of a linear correction versus an approach to saturation correction at 70%, 80%, and 90% of the peak field. A schematic outline of the decision process is shown in Figure 9.

The first step is to perform a lack-of-fit *F* test for whole loop linearity using the data before slope correction (Jackson & Solheid, 2010). This test assesses if the lack of fit between the data and a linear model fit to the whole loop is significant. If the *p* value of this test is $<0.05$ (5% significance level) then we can reject the null hypothesis that the misfit between the data and a linear loop is due to random noise, hence conclude that it is primarily due to a lack of fit (i.e., the loop is not linear). If the null hypothesis cannot be rejected (i.e., $p \geq 0.05$ indicating that the whole loop appears linear) then no high-field slope correction is applied.

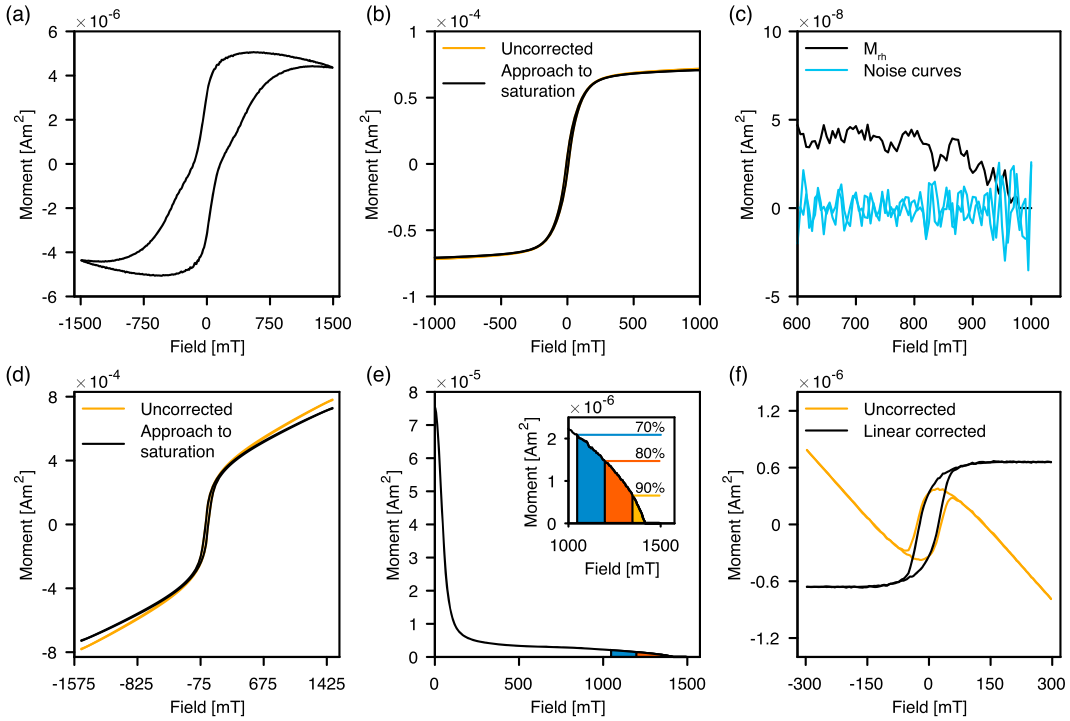


**Figure 10.** Examples of high-field slope corrections. (a) An oxidized granite specimen with mixed high- and low-coercivity components yields a hysteresis loop that remains open at high-fields. Currently, no high-field slope correction is strictly valid for such a loop. (b) A hysteresis loop of volcanic chip before and after automatic correction, which applies an approach to saturation correction. (c) The high-field averaged $M_{rh}$ curve and high-field portions of the noise curve (negative field half inverted to positive fields) for the loop in panel (b). At 70%, 80%, and 90% of the peak field (700, 800, and 900 mT, respectively), $M_{rh}$ signal-to-ratios are 10.6, 7.8, and 1.9 dB, respectively. (d) A hysteresis loop of a thermally stabilized basalt before and after automatic correction, which applies an approach to saturation correction. (e) The averaged $M_{rh}$ curve for the loop in panel (d), where the high-field portions used to calculate high-field to total $M_{rh}$ signal ratios are shaded in color. The inset enlarges the high-field region. The HAR values at 70%, 80%, and 90% of the peak field are −24.7, −32.4, and −50.1 dB, respectively. Above 90% of the peak field, the loop can be considered closed. (f) An MTB specimen with a strong diamagnetic component. The automatic correction favors loop closure and a linear high-field slope correction.

If a linear loop is rejected, HystLab assesses whether the loop is closed at high-fields. Loops that are distinctly open at high-fields indicate that a specimen is not saturated and not in the approach to saturation regime (e.g., Figure 10a). In such cases, no form of high-field slope correction can currently be applied.

Here we introduce two new statistics to assess loop closure at high-fields. First, at a given field above which closure is to be tested, the SNR of the high-field $M_{rh}$ curve to high-field noise is assessed—an open loop will have a nonzero $M_{rh}$ curve over the defined high-field range, which should be distinctive above the noise (i.e., have a high SNR). To assess the $M_{rh}$ signal, the negative field $M_{rh}$ curve is inverted around the origin and averaged with the positive field half and all negative moments are set to zero (after drift has been appropriately correct for, negative values are a result of noise and setting them to zero removes them from the estimation of signal power). The $M_{rh}$ signal power is taken as the RMS of this average $M_{rh}$ curve. The power of the noise is taken as the RMS of the high-field noise and the SNR is calculated in decibels as $20 \times \log_{10}$ (signal/noise). High values of SNR indicate that the nonzero nature of the $M_{rh}$ curve is distinct above the noise and indicate that the loop may be open.

The second statistic assesses the relative contribution of the high-field $M_{rh}$ signal to the entire $M_{rh}$ signal. A perfectly closed loop will have zero area under the high-field portion of the $M_{rh}$ curve, but for most real data measurements the high-field $M_{rh}$ is nonzero and a level tolerance is needed to assess loop closure. To assess this, we define the high-field area ratio (HAR), which is the ratio of the area under the high-field $M_{rh}$ curve to the area under the entire $M_{rh}$ curve. The areas are calculated using the averaged $M_{rh}$ curve described above and, following the SNR calculation, HAR is calculated in dB. High values of HAR indicate that the high-field portion of the $M_{rh}$ curve forms a notable part of the total curve and indicate that the loop may be open;

extremely low values indicate that the high-field contribution is small and the loop may reasonably be assumed to be closed.

The automatic correction determines that a loop is closed if the SNR is less than 8 dB or the HAR is less than −48 dB. An 8 dB SNR corresponds to an average $M_{rh}$ signal ~2.5 times stronger than the noise, while an HAR of −48 dB corresponds to a high-field area ~1/250th of the total $M_{rh}$ area. These thresholds tend to prefer loop closure, for which high-field slope correction methods are viable. For loops where closure is rejected, no correction is applied and the user should manually consider the appropriateness of high-field slope corrections.

Figure 10a is an example of an open loop for which no correction can be rigorously applied. At 90% of the peak field, SNR = 15.8 dB and HAR = −47.8 dB. It is possible to test for closure at higher peak fields, but it should be kept in mind that even minor loops that are far from saturation will close at their peak field. Therefore, any loop will appear closed near the peak field.

In Figure 10b we show a hysteresis loop that visually appears to close at high-fields. The corresponding high-field $M_{rh}$ and noise curves are shown in Figure 10c. At 70%, 80%, and 90% of the peak field (700, 800, and 900 mT, respectively), $M_{rh}$ SNR values are 10.6, 7.8, and 1.9 dB, respectively. Above 80% of the peak field, the SNR falls just below our threshold of 8 dB and, because $M_{rh}$ becomes comparable to the level of noise, the loop can be considered closed. HAR at the three field levels are −32.5, −38.0, and −49.4 dB.

In Figure 10d we show another loop that visually appears to be closed. In this case, the SNR values at 70%, 80%, and 90% of the peak field are all >19.3 dB. The averaged $M_{rh}$ curve is shown in Figure 10e and the high-field areas are highlighted. The high-field regions have HAR values −24.7, −32.4, and −50.1 dB for 70%, 80%, and 90% of the peak field, respectively. These correspond to total $M_{rh}$ areas 17, 42, and 320 times larger than the respective high-field regions. The high SNR values indicate that the high-field $M_{rh}$ segments are not unduly affected by noise, but the extremely low HAR value at 90% peak field indicates that the high-field $M_{rh}$ signal is small and it is reasonable to assume loop closure.

If an open loop is rejected, HystLab further tests the linearity of the high-field portion of the hysteresis loop to evaluate whether a loop is saturated or approaching saturation (cf. Jackson & Solheid, 2010]. For a given field above which the specimen is assumed to be saturated or approaching saturation, two styles of *F* test are performed to assess which mode of slope correction should be applied. First, a linear model is fitted to the high-field data. Using the negative high-field data as replicates of the positive high-field data, we perform a lack-of-fit *F* test to test the null hypothesis that the misfit between the data and the model can be explained by the noise of the data. If the *p* value of this test is <0.05 (5% significance level), then we reject the null hypothesis. That is, the poor fit of a linear model to the high-field data cannot be explained by noise and may be better explained by an alternative model (i.e., approach to saturation).

The second test is an *F* test comparison between the variance accounted for by a linear model (with two free parameters) and the variance accounted for by an approach to saturation model (with four free parameters). If the *p* value of this test is <0.05 (5% significance level), then we reject the null hypothesis that the simpler linear model fits the data adequately and conclude that the more complex approach to saturation model is justified.

If one or both of these *F* tests come out in favor of a linear high-field slope, a linear high-field correction is applied. Only if both tests reject linearity is an approach to saturation correction applied. This automated approach tends to favor applying a linear high-field slope correction because of the ill-conditioned nature of the approach to saturation correction (see Jackson & Solheid, 2010 for a full discussion of the challenges of applying an approach to saturation correction). We note that the *F* tests are for general guidance and can be influenced by the smoothing introduced by loop interpolation and drift corrections. For specimens where the automated correction suggests approach to saturation, we recommend consideration of the physical validity of the correction and a careful inspection and manual checking of fields around the field above which the correction is applied. Furthermore, if possible, measuring hysteresis to higher peak fields can help better resolve the saturation regime of many specimens.

The loops shown in Figures 10b and 10d are examples where a linear high-field slope is rejected and an approach to saturation correction is applied. In Figure 10f we show a hysteresis loop from an MTB specimen with a strong diamagnetic signal (the offset-corrected loop shown in Figure 7a). Both *F* tests cannot reject a linear high-field slope; hence, a linear correction is applied.

### 4.6. Loop Fitting

During data processing, HystLab also fits the hysteresis loops following similar procedures to von Dobeneck (1996) and Jackson and Solheid (2010). These fitted loops can be used to estimate the hysteresis parameters from noisy data but are not a substitute for re-measuring extremely noisy data. How well the model fits the observed data is assessed by a lack-of-fit *F* test (Jackson & Solheid, 2010).

First, the remanent ($M_{rh}$) and induced ($M_{ih}$) hysteretic curves are calculated (von Dobeneck, 1996). The negative field halves are inverted and averaged with the positive field halves to reduce noise—HystLab fits to these averaged half curves. Like Jackson and Solheid (2010), HystLab fits a combination of hyperbolic and sigmoid logistic basis functions to the $M_{rh}$ and $M_{ih}$ curves. In HystLab, however, the basis functions are not a predefined set but are defined for each specimen such that the median fields of the basis functions correspond to equally spaced moments on the $M_{rh}$ and $M_{ih}$ curves.

For each curve, a maximum of 22 basis functions are fitted, for a total maximum of 44 per hysteresis loop. The $M_{rh}$ curve is fitted with 10 hyperbolic secant functions, 10 sigmoid logistic functions, and 2 linear functions with positive and negative slopes. The $M_{ih}$ curve is fitted with 10 hyperbolic tangent functions, 10 sigmoid logistic functions, and 2 linear functions (to account for any paramagnetic and diamagnetic components of uncorrected loops). The mathematical form of the basis functions is given in the HystLab instruction manual (see also Jackson & Solheid, 2010; von Dobeneck, 1996). Where insufficient data are available to perform the lack-of-fit *F* test, HystLab reduces the number of hyperbolic and sigmoid functions to less than 10 each.

The relative contribution of the basis functions is estimated using the sparse unmixing by variable splitting and augmented Lagrangian (SUnSAL) algorithm of Bioucas-Dias (2009). In addition to the sparsity enforced by SUnSAL, basis functions with a relative contribution of $<0.01\%$ are omitted from the final fit to minimize the total number of used functions.

The quality of the fit is assessed using the *F* test for lack-of-fit (Jackson & Solheid, 2010). This lack-of-fit test, which is performed on the whole hysteresis loop, tests the null hypothesis that the misfit between the model and the data can be attributed to independent and identically distributed. Gaussian noise. If the *p* value of this test is $<0.05$ (5% significance level), then we can reject the null hypothesis. That is, the poor fit of the basis functions to the loop cannot be explained by noise. In these cases, the quality of the data should be sufficient to estimate the various hysteresis statistics from the data directly. Users should consider each specimen carefully and note the *F* test results are for guidance and can be influenced by the smoothing introduced by loop interpolation and drift corrections.

In Figure 11a, we show an example of a visibly noisy loop and its fit (the loop is one of the 30 repeated loops measured in continuous mode with 100 ms averaging described in section 3.1). In Figure 11b we also show a higher quality, lower noise loop from the same specimen alongside the fit to the loop in Figure 11a (the lower noise loop is the average of the 30 loops measured in discrete field sweep mode with a pause time of 300 ms and 200 ms averaging time). The RMS misfit between the measured loop and the averaged loop is $2.03 \times 10^{-8}$ Am$^2$ and the RMS misfit between the loop fit and the averaged loop is $1.40 \times 10^{-8}$ Am$^2$, indicating that the fit to the lower quality data is a better estimate of the higher quality loop. In Figure 11c we plot the density distributions of the RMS misfits between higher quality averaged loop and (1) the 30 noisier loops and (2) the model fits to the 30 noisier loops. For 24 of the 30 loops the model fit more accurately represents the lower noise loop than the measured data, which illustrates how fitting hysteresis loops can help to filter noisy data.

Fitting loops can also be a useful diagnostic tool for determining appropriate processing for noisy or otherwise problematic loops. The hysteresis loops for a weak carbonate specimen (Jackson & Swanson-Hysell, 2012) after positive field drift correction and after upper branch correction are shown in Figure 11d (a linear high-field slope correction has been applied to both loops); the loop closure errors are $7.03 \times 10^{-9}$ Am$^2$ and $7.60 \times 10^{-9}$ Am$^2$, respectively. Note the upward and downward curvature in strong positive and negative fields, respectively. In the absence of a metamagnetic transition, such curvature can be assumed to be the result of an unknown experimental artifact. A comparison between the fits to these two loops is shown in Figure 11e. The fit to the positive field drift corrected loop does not close (parallel and nonintersecting high-field upper and lower branches; inset Figure 11e), but the fit to the upper branch corrected loop yields a more closed loop, indicating it is a more appropriate drift correction to apply for this specimen.

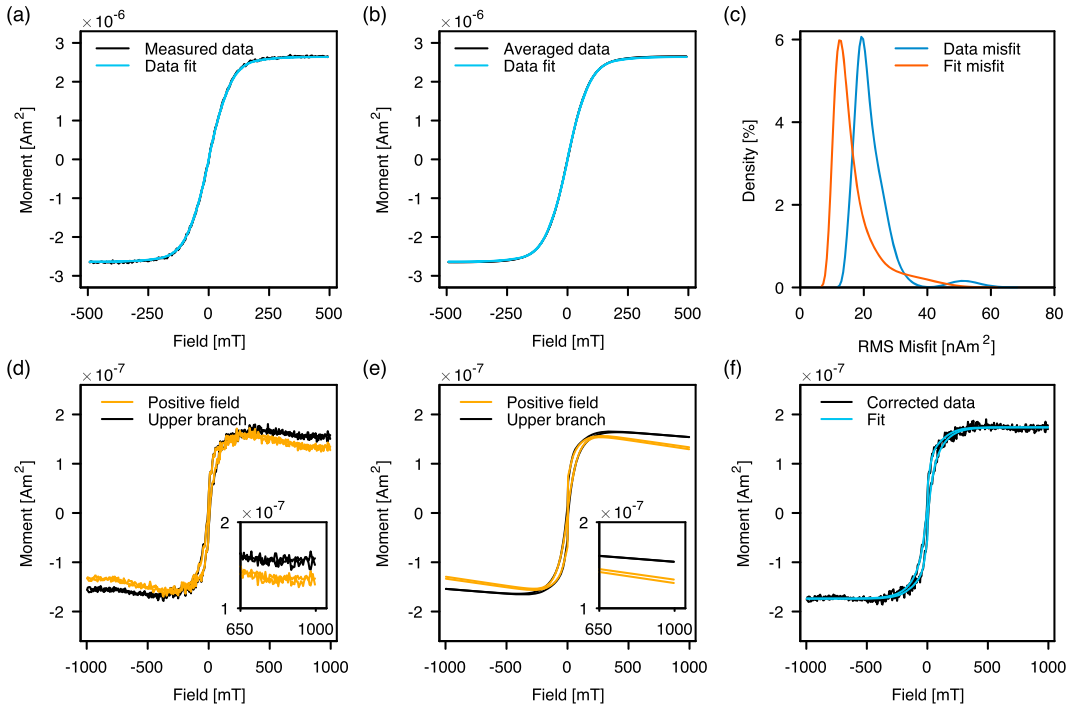


**Figure 11.** Examples of hysteresis loop fitting. (a) Fitting of a loop measured with a 100 ms averaging time in continuous sweep mode. (b) The average of 30 loops for the same specimen in panel (b), but measured with a 200 ms averaging time in discrete sweep mode with 200 ms settling time. The fitted loop is the same as shown in panel (a). (c) The distribution of misfits between 30 replicates of the loop shown in panel (a) and the averaged loop in panel (b, blue curve) and the distribution of misfits between the model fits to the 30 repeat loops and the averaged loop in part (b, orange curve). Twenty-four of the 30 replicates have model fits that more accurately represent the higher quality loop than the original measurements. (d) A weak carbonate specimen after positive field and upper branch drift corrections, both of which yield apparently similarly closed loops. The high-field region is expanded in the inset. (e) Fitting results of the loops shown in (d) reveal a distinct lack of loop closure after positive field drift correction. The high-field region is expanded in the inset. (f) Using the high-field segment of the fitted loop yields a better linear slope correction than using the data directly.

In both cases, however, the high-field slope correction underestimates the high-field diamagnetic susceptibility. As a consequence, after linear high-field slope corrections, both loops and their fits have negative high-field slopes—the correction is inadequate. This incomplete correction is due to unusual high-field drift, present in all four high-field segments, that results in slight anomalous curvature of the high-field segments (Figure 11d). HystLab provides the option to apply slope correction and estimate loop parameters for the fitted loop in addition to the measured data. The resultant loop after upper branch drift correction using the fitted loop to correct the high-field slope with a linear correction is shown in Figure 11f. Applying the slope correction to the fitted loop yields more satisfactory high-field behavior that fully corrects for the diamagnetic component.

Fitting a noisy hysteresis loop can have a number of advantages, including removing high-frequency noise as well as a means of assessing the appropriateness of processing and correcting high-field slope behavior. We emphasize, however, that although fitting can help to analyze noisy data, it is no substitute for remeasuring extremely noisy hysteresis loops.

## 5. HystLab Features

### 5.1. Supported Data

Within the rock and paleomagnetic community, a range of magnetometers can be used to measure hysteresis loop data. These include VSMs, alternating gradient magnetometers, variable field translation balances, as well as superconducting quantum interference device magnetometers coupled with high-field magnets.

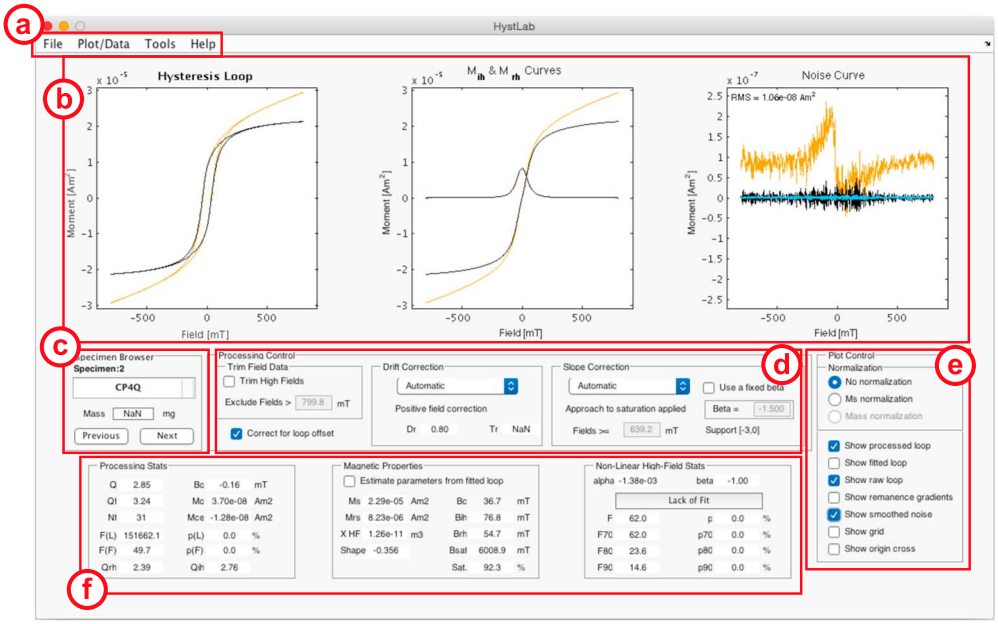


**Figure 12.** The main HystLab interface. (a) The menu bar for loading data and exporting results and plots. (b) The main data plots. (c) Specimen browser. (d) The processing control panel. (e) The plot control panel. (f) The analysis results and statistics.

This variety, combined with a range of manufacturers, means that numerous data formats are available, which can complicate consistent analysis.

HystLab supports the most widely used data formats including multiple format versions for the Princeton Measurements Corporation MicroMag 3900 VSM and 2900 alternating gradient magnetometer, Lake Shore 7400 and 8600 VSMs, Quantum Designs Magnetic Properties Measurement System, magnetic measurements variable field translation balances, and MicroSense VSMs. HystLab allows users to append data to the current session, which allows multiple data formats to be loaded and analyzed together. Once data are loaded into HystLab users can save their HystLab session, allowing them to complete their analyses at a later date or to share their results with collaborators. If any users encounter an unsupported data format, they should contact the authors with an example file and it will be added to HystLab.

### 5.2. Interface

The main HystLab window is shown in Figure 12. Data can be loaded via the menu bar (Figure 12a) and will be plotted in the three main plots (Figure 12b). Here the original raw data can be plotted alongside the processed data as well as the fitted data. In addition to the hysteresis loop, the remanent ($M_{rh}$) and induced ($M_{ih}$) hysteretic curves, as well as the noise curve are also shown (Figure 12b). Multiple specimens can be loaded at once and the user can browse through each (Figure 12c). On loading data, loops are processed to correct for offset and apply the automatic drift and high-field slope corrections. Additional processing can then be performed on a specimen-by-specimen basis using the control panel shown in Figure 12d. The plot control panel (Figure 12e) allows for different moment/magnetization normalizations as well as controlling which data are displayed. Figure 12f contains the analysis results and statistics—a comprehensive list and description of each statistic can be found in the HystLab documentation (accessible through the *Help* menu, Figure 12a).

### 5.3. Data and Plots

Statistics and analysis parameters in HystLab can be exported to tab delimited text files. The default plot color schemes are chosen to enhance contrast for colorblind users (Wong, 2011), but are fully customizable and can be saved to a user preference file for future use. In addition, by clicking on each plot, a new MATLAB

figure window will open, which allows further customization. All plots presented in HystLab can be exported to encapsulated postscript files that are publication ready with little or no adjustment.

## 6. Summary

Magnetic hysteresis loops are one of the most ubiquitous rock magnetic measurements in the Earth magnetism community. These rapid to measure data provide a diverse variety of descriptive statistics that have a broad range of applications. However, despite their apparent ease and simplicity, in-depth and quantitative descriptions of measuring and processing hysteresis loops to avoid or correct for widely occurring detrimental factors (e.g., drift and loop offset) are rarely performed.

Here we have outlined a range of approaches that can be used to improve the measurement quality of hysteresis loops. Although these are largely developed from extensive experience using VSM systems, many are applicable to a wide range of instruments used to measure magnetic hysteresis. These strategies are also valid for other types of data measurable on the same equipment (e.g., isothermal remanent magnetization acquisition, back-field demagnetization, first-order reversal curves, among others).

Building on established processing recommendations, we have developed HystLab, which is a new software package for the advanced processing and analysis of hysteresis loop data. Supporting a wide range of data formats, with the ability to export data and generate publication ready figures, HystLab has a range of tools to correct for commonly occurring negative artifacts in hysteresis data. We hope that HystLab can enhance both productivity and accuracy when processing and analyzing large data sets, and we encourage users with suggestions or bug reports to contact us and help to improve the software.

## Appendix A: Glossary of Hysteresis Statistics and Parameters

Below is a brief glossary of the major terms used in this paper. Further details and definitions are given in the documentation that accompanies HystLab.

- $\alpha$ The alpha parameter for the applied approach to saturation high-field slope correction (Fabian, 2006; Jackson & Solheid, 2010).
- $\beta$ The beta parameter for the applied approach to saturation high-field slope correction (Fabian, 2006; Jackson & Solheid, 2010).
- $B_0$ Hysteresis loop offset along the field (horizontal) axis.
- $B_c$ Hysteresis loop coercivity.
- $B_{ih}$ The median value of the induced hysteretic curve (von Dobeneck, 1996).
- $B_{rh}$ The median value of the remanent hysteretic curve (von Dobeneck, 1996).
- HAR The high-field area ratio. The ratio (in dB) of the area under the high-field $M_{rh}$ curve to the area under the entire $M_{rh}$ curve.
- $M_0$ Hysteresis loop offset along the moment/magnetization (vertical) axis.
- $M_{ce}$ Hysteresis loop closure error (Jackson & Solheid, 2010). This is calculated as the difference between the moment of the initial positive field and the moment in the final positive field.
- $M_f$ Ferromagnetic moment/magnetization at a specific field.
- $M_{ih}$ The induced hysteric moment/magnetization curve (Rivas et al., 1981; von Dobeneck, 1996). Calculated as half the sum of the upper and lower hysteresis branches.
- $M_p$ Paramagnetic moment/magnetization at a specific field.
- $M_{rh}$ The remanent hysteric moment/magnetization curve (Rivas et al., 1981; von Dobeneck, 1996). Calculated as half the difference of the upper and lower hysteresis branches.
- $M_{rs}$ Saturation remanent moment/magnetization.
- $M_s$ Saturation moment/magnetization.
- $Q$ A measure of the quality of the raw hysteresis loop determined by taking the linear correlation between the upper and inverted lower branches.
- $Q_f$ A measure of the quality of the slope-corrected (ferromagnetic) hysteresis loop determined by taking the linear correlation between the upper and inverted lower branches.
- $Q_{ih}$ A measure of the quality of the processed $M_{ih}$ curve determined by taking the linear correlation between the positive field half and the inverted negative field half.
- $Q_{rh}$ A measure of the quality of the processed $M_{rh}$ curve determined by taking the linear correlation between the positive field half and the reflected negative field half.

| | |
|---|---|
| Shape | Hysteresis loop shape factor, σ (Fabian, 2003). |
| SNR | The signal-to-noise ratio (in dB) of the high-field $M_{rh}$ to the high-field noise. |
| $T_0$ | The initial temperature of a specimen at the beginning of a measurement. |
| $T_A$ | The ambient temperature between the pole pieces of the measurement equipment. |
| $T_r$ | The ratio of the specimen initial temperature ($T_0$) to the ambient temperature between the pole pieces ($T_A$). Estimated for the paramagnetic drift correction. |
| $X_{HF}$ | High-field susceptibility (determined from the high-field slope correction). |

**Acknowledgments**
We thank Andy Biggin, Liao Chang, Cao Changqian, Mimi Hill, Jinhua Li, Suzhen Liu, Adrian Muxworthy, Eduard Petrovsky, Daniele Thallner, Yuhji Yamamoto, and Lake Shore Cryotronics for providing test data. Richard Bono and Peat Solheid are thanked for their thoughts and discussion. We are very grateful to Harry Reichard and Brad Dodrill of Lake Shore Cryotronics for their valuable discussion on this work and their help and advice over many years. G. A. P. acknowledges funding from a NERC Independent Research Fellowship (NE/P017266/1) and NSFC grants 41574063 and 41621004, and CAS project XDB18010203. M. J. acknowledges support of the Institute for Rock Magnetism, funded by the NSF Instruments and Facilities program and by the University of Minnesota. The data presented here are available with the HystLab software package (https://github.com/greigpaterson/HystLab).

## References

Bioucas-Dias, J. M. (2009). A variable splitting augmented Lagrangian approach to linear spectral unmixing. In *First IEEE GRSS workshop on Hyperspectral Image and Signal Processing: WHISPERS 2009* (pp. 1–4). Grenoble, France: IEEE. https://doi.org/10.1109/WHISPERS.2009.5289072

Carvallo, C., Roberts, A. P., Leonhardt, R., Laj, C., Kissel, C., Perrin, M., & Camps, P. (2006). Increasing the efficiency of paleointensity analyses by selection of samples using first-order reversal curve diagrams. *Journal of Geophysical Research*, *111*, B12103. https://doi.org/10.1029/2005JB004126

Chang, L., Bolton, C. T., Dekkers, M. J., Hayashida, A., Heslop, D., Krijgsman, W., et al. (2016). Asian monsoon modulation of nonsteady state diagenesis in hemipelagic marine sediments offshore of Japan. *Geochemistry, Geophysics, Geosystems*, *17*, 4383–4398. https://doi.org/10.1002/2016GC006344

Chen, A., Egli, R., & Moskowitz, B. M. (2005). A FORC in the road? *IRM Quarterly*, *15*, 8–11.

Dodrill, B. C. (2001). The performance of the model 7400 VSM: Sensitivity. Retrieved from http://www.lakeshore.com/Documents/ThePerformanceoftheModel7400VSMSensitivity.pdf, (accessed Nov. 2017).

Fabian, K. (2003). Some additional parameters to estimate domain state from isothermal magnetization measurements. *Earth and Planetary Science Letters*, *213*(3-4), 337–345. https://doi.org/10.1016/S0012-821X(03)00329-7

Fabian, K. (2006). Approach to saturation analysis of hysteresis measurements in rock magnetism and evidence for stress dominated magnetic anisotropy in young mid-ocean ridge basalt. *Physics of the Earth and Planetary Interiors*, *154*(3-4), 299–307. https://doi.org/10.1016/j.pepi.2005.06.016

Haag, M., Dunn, J. R., & Fuller, M. D. (1995). A new quality check for absolute palaeointensities of the Earth magnetic field. *Geophysical Research Letters*, *22*, 3549–3552. https://doi.org/10.1029/95GL03333

Harrison, R. J., McEnroe, S. A., Robinson, P., Carter-Stiglitz, B., Palin, E. J., & Kasama, T. (2007). Low-temperature exchange coupling between $Fe_2O_3$ and $FeTiO_3$: Insight into the mechanism of giant exchange bias in a natural nanoscale intergrowth. *Physical Review B*, *76*(17), 174436. https://doi.org/10.1103/PhysRevB.76.174436

Hatfield, R. G., Stoner, J. S., Reilly, B. T., Tepley, F. J., Wheeler, B. H., & Housen, B. A. (2017). Grain size dependent magnetic discrimination of Iceland and South Greenland terrestrial sediments in the northern North Atlantic sediment record. *Earth and Planetary Science Letters*, *474*, 474–489. https://doi.org/10.1016/j.epsl.2017.06.042

Housen, B. A., Banerjee, S. K., & Moskowitz, B. M. (1996). Low-temperature magnetic properties of siderite and magnetite in marine sediments. *Geophysical Research Letters*, *23*, 2843–2846. https://doi.org/10.1029/96GL01197

Jackson, M., & Solheid, P. (2010). On the quantitative analysis and evaluation of magnetic hysteresis data. *Geochemistry, Geophysics, Geosystems*, *11*, Q04Z15. https://doi.org/10.1029/2009GC002932

Jackson, M., & Swanson-Hysell, N. L. (2012). Rock magnetism of remagnetized carbonate rocks: another look. In *Remagnetization and Chemical Alteration of Sedimentary Rocks* (pp. 229–251). Geological Society, London. https://doi.org/10.1144/sp371.3

Kissel, C., Guillou, H., Laj, C., Carracedo, J. C., Nomade, S., Perez-Torrado, F., & Wandres, C. (2011). The Mono Lake excursion recorded in phonolitic lavas from Tenerife (Canary Islands): Paleomagnetic analyses and coupled K/Ar and Ar/Ar dating. *Physics of the Earth and Planetary Interiors*, *187*(3-4), 232–244. https://doi.org/10.1016/j.pepi.2011.04.014

Krása, D., Wilkinson, C. D. W., Gadegaard, N., Kong, X., Zhou, H., Roberts, A. P., et al. (2009). Nanofabrication of two-dimensional arrays of magnetite particles for fundamental rock magnetic studies. *Journal of Geophysical Research*, *114*, B02104. https://doi.org/10.1029/2008JB006017

Lagarias, J., Reeds, J., Wright, M., & Wright, P. (1998). Convergence properties of the Nelder-Mead simplex method in low dimensions. *SIAM Journal on Optimization*, *9*(1), 112–147. https://doi.org/10.1137/S1052623496303470

Li, J., Pan, Y., Liu, Q., Yu-Zhang, K., Menguy, N., Che, R., et al. (2010). Biomineralization, crystallography and magnetic properties of bullet-shaped magnetite magnetosomes in giant rod magnetotactic bacteria. *Earth and Planetary Science Letters*, *293*(3-4), 368–376. https://doi.org/10.1016/j.epsl.2010.03.007

Li, J., Wu, W., Liu, Q., & Pan, Y. (2012). Magnetic anisotropy, magnetostatic interactions and identification of magnetofossils. *Geochemistry, Geophysics, Geosystems*, *13*, Q10Z51. https://doi.org/10.1029/2012GC004384

Li, S., Yang, Z., Deng, C., He, H., Qin, H., Sun, L., et al. (2017). Clockwise rotations recorded in redbeds from the Jinggu Basin of northwestern Indochina. *Geological Society of America Bulletin*, https://doi.org/10.1130/b31637.1

Lin, W., & Pan, Y. (2009). Uncultivated magnetotactic cocci from Yuandadu Park in Beijing, China. *Applied and Environmental Microbiology*, *75*(12), 4046–4052. https://doi.org/10.1128/aem.00247-09

Liu, S., Deng, C., Xiao, J., Li, J., Paterson, G. A., Chang, L., et al. (2015). Insolation driven biomagnetic response to the Holocene warm period in semi-arid East Asia. *Scientific Reports*, *5*(1), 8001. https://doi.org/10.1038/srep08001

Liu, S., Deng, C., Xiao, J., Li, J., Paterson, G. A., Chang, L., et al. (2016). High-resolution enviromagnetic records of the last deglaciation from Dali Lake, Inner Mongolia. *Palaeogeography Palaeoclimatology Palaeoecology*, *454*, 1–11. https://doi.org/10.1016/j.palaeo.2016.04.030

Muxworthy, A. R., Bland, P. A., Davison, T. M., Moore, J., Collins, G. S., & Ciesla, F. J. (2017). Evidence for an impact-induced magnetic fabric in Allende, and exogenous alternatives to the core dynamo theory for Allende magnetization. *Meteoritics and Planetary Science*, *52*(10), 2132–2146. https://doi.org/10.1111/maps.12918

Muxworthy, A. R., Heslop, D., Paterson, G. A., & Michalk, D. (2011). A Preisach method for estimating absolute paleofield intensity under the constraint of using only isothermal measurements: 2. Experimental testing. *Journal of Geophysical Research*, *116*, B04103. https://doi.org/10.1029/2010JB007844

Muxworthy, A. R., Matzka, J., & Petersen, N. (2001). Comparison of magnetic parameters of urban atmospheric particulate matter with pollution and meteorological data. *Atmospheric Environment*, *35*(26), 4379–4386. https://doi.org/10.1016/S1352-2310(01)00250-3

Pan, Y., Petersen, N., Davila, A. F., Zhang, L., Winklhofer, M., Liu, Q., et al. (2005). The detection of bacterial magnetite in recent sediments of Lake Chiemsee (southern Germany). *Earth and Planetary Science Letters*, *232*(1-2), 109–123. https://doi.org/10.1016/j.epsl.2005.01.006

Paterson, G. A., Heslop, D., & Pan, Y. (2016). The pseudo-Thellier palaeointensity method: New calibration and uncertainty estimates. *Geophysical Journal International*, *207*(3), 1596–1608. https://doi.org/10.1093/gji/ggw349

Paterson, G. A., Muxworthy, A. R., Roberts, A. P., & Mac Niocaill, C. (2010). Assessment of the usefulness of lithic clasts from pyroclastic deposits for paleointensity determination. *Journal of Geophysical Research*, *115*, B03104. https://doi.org/10.1029/2009JB006475

Paterson, G. A., Muxworthy, A. R., Yamamoto, Y., & Pan, Y. (2017). Bulk magnetic domain stability controls paleointensity fidelity. *Proceedings of the National Academy of Sciences of the United States of America*, *114*(50), 13,120–13,125. https://doi.org/10.1073/pnas.1714047114

Paterson, G. A., Wang, Y., & Pan, Y. (2013). The fidelity of paleomagnetic records carried by magnetosome chains. *Earth and Planetary Science Letters*, *383*, 82–91. https://doi.org/10.1016/j.epsl.2013.09.031

Rivas, J., Zamarro, J., Martin, E., & Pereira, C. (1981). Simple approximation for magnetization curves and hysteresis loops. *IEEE Transactions on Magnetics*, *17*(4), 1498–1502. https://doi.org/10.1109/TMAG.1981.1061241

Tikoo, S. M., Weiss, B. P., Shuster, D. L., Suavet, C., Wang, H., & Grove, T. L. (2017). A two-billion-year history for the lunar dynamo. *Science Advances*, *3*(8), e1700207. https://doi.org/10.1126/sciadv.1700207

Van Hinsbergen, D. J. J., Straathof, G. B., Kuiper, K. F., Cunningham, W. D., & Wijbrans, J. (2008). No vertical axis rotations during Neogene transpressional orogeny in the NE Gobi Altai: Coinciding Mongolian and Eurasian early cretaceous apparent polar wander paths. *Geophysical Journal International*, *173*(1), 105–126. https://doi.org/10.1111/j.1365-246X.2007.03712.x

von Dobeneck, T. (1996). A systematic analysis of natural magnetic mineral assemblages based on modelling hysteresis loops with coercivity-related hyperbolic basis functions. *Geophysical Journal International*, *124*(3), 675–694. https://doi.org/10.1111/j.1365-246X.1996.tb05632.x

Williams, W., Evans, M. E., & Krása, D. (2010). Micromagnetics of paleomagnetically significant mineral grains with complex morphology. *Geochemistry, Geophysics, Geosystems*, *11*, Q02Z14. https://doi.org/10.1029/2009GC002828

Wong, B. (2011). Color blindness. *Nature Methods*, *8*(6), 441–441. https://doi.org/10.1038/nmeth.1618

Zhang, C., Appel, E., & Qiao, Q. (2013). Heavy metal pollution in farmland irrigated with river water near a steel plant—Magnetic and geochemical signature. *Geophysical Journal International*, *192*(3), 963–974. https://doi.org/10.1093/gji/ggs079

Zhang, R., Necula, C., Heslop, D., & Nie, J. (2016). Unmixing hysteresis loops of the late Miocene–early Pleistocene loess-red clay sequence. *Scientific Reports*, *6*(1), 29515. https://doi.org/10.1038/srep29515